# Multi-step and Elastically-stable Mechanical Metamaterials

**Lianchao Wang[1,2,4], Julio A. Iglesias Martínez[2], Krzysztof K. Dudek[2,3], Gwenn Ulliac[2], Xinrui Niu[4], Yajun Zou[1], Bing Wang[1,*], Vincent Laude[2,*], and Muamer Kadic[2,*]**

[1]National Key Laboratory of Science and Technology on Advanced Composites in Special Environments, Harbin Institute of Technology, Harbin, 150001, PR China
[2]Université de Franche-Comté, CNRS, Institut FEMTO-ST, Besançon, 25000, France
[3]Institute of Physics, University of Zielona Gora, ul. Szafrana 4a, 65-069 Zielona Gora, Poland
[4]Department of Mechanical Engineering, City University of Hong Kong, Hong Kong SAR, PR China
[*]e-mail: wangbing86@hit.edu.cn
[*]e-mail: vincent.laude@femto-st.fr
[*]e-mail: muamer.kadic@univ-fcomte.fr

## ABSTRACT

Materials and structures with tunable mechanical properties are essential for numerous applications. However, constructing such structures poses a great challenge since it is normally very complicated to change the properties of a material after its fabrication, particularly in pure force fields. Herein, we propose a multi-step and elastically stable 3D mechanical metamaterial having simultaneously tunable effective Young's modulus and auxeticity controlled by the applied compressive strain. Metamaterial samples are fabricated by 3D printing at the centimetric scale, with selective laser sintering, and at the micrometric scale, with two-photon lithography. Experimental results indicate an elementary auxeticity for small compressive strains but superior auxeticity for large strains. Significantly, the effective Young's modulus follows a parallel trend, becoming larger with increasing compressive strain. A theoretical model explains the variations of the elastic constants of the proposed metamaterials as a function of geometry parameters and provides a basic explanation for the appearance of the multi-step behavior. Furthermore, simulation results demonstrate that the proposed metamaterial has the potential for designing metamaterials exhibiting tunable phononic band gaps. The design of re-usable elastically-stable multi-step metamaterials, with tunable mechanical performances supporting large compression, is made possible thanks to their delocalized deformation mode.

## 1 Introduction

Over the last decade, metamaterials have been rising exponentially[1–5] and even more so for mechanical metamaterials[6–24, 24–27] thanks to new fabrication techniques such as 3D printing[28–34]. Generally, after the manufacturing process, the mechanical behavior of a metamaterial is set and is hardly modified[35–37]. Nevertheless, materials and structures with varying static or dynamical mechanical properties are attractive to many engineering fields[7, 35, 38–43]. To implement them, numerous methods have been proposed and many metamaterials and meta-structures with tunable mechanical behaviors have been investigated. For instance, Janbaz *et al.*[38] proposed a bi-beam that consists of two beams with different viscoelasticity to design metamaterials with strain-rate-dependent mechanical behavior. Liang *et al.*[44] used magnetic interactions to change globally the energy and thus the configuration of a system. Mü *et al.*[42] investigated a metamaterial with different auxeticity under varying optical stimuli. Ji *et al.*[45] used a bi-material beam showing varying mechanical response as a function of temperature for soft micro-robotic applications. Farzaneh *et al.*[46] proposed a sequential metamaterial with alternating Poisson's ratios. Dudek *et al.*[47] used magnetic inclusions to reconfigure a structure and tune the mechanical performance of the entire system. Wang *et al.*[48] demonstrated a metamaterial that exhibits a change in the sign of the effective tangent Poisson's ratio during compression, without significant enhancement in Young's modulus.

There are three main principles to design metamaterials with tunable mechanical properties, i.e., the principle of structural instabilities and material post-buckling[49, 50], the use of multi-body systems[39, 51, 52], and the theory of multi-material systems[42, 47]. In principle, these methods are efficient for obtaining metamaterials with tunable mechanical behaviors. Nevertheless, some additional limitations are introduced, for instance, global elastic instabilities of the whole system, excess challenges for fabrication technology, demanding requirements for multi-physical fields, etc. Furthermore, most previous studies have focused on a single adjustable mechanical property[48], implying that the adjustability of other mechanical parameters of the metamaterial has been ignored or sacrificed. Indeed, materials with several tunable mechanical parameters in different states can introduce multiple functionalities.

As two fundamental and significant mechanical properties of materials, the Young's modulus and the Poisson's ratio (in particular if the latter value is negative, i.e., for auxeticity) play essential roles in material investigations and applications[6,36,39,43,53–55]. Mechanical metamaterials with simultaneously tunable Young's modulus and auxeticity have rarely been reported but are highly desirable and offer a significant commercial appeal. For instance, in the case of applications requiring the tunable load-bearing capacity and volume change at the same time, it is essential to harness the ability to design materials with both of these mechanical properties being adjustable. In this regard, we consider in this work a single constituent material to design a mechanical metamaterial that shows elastically stable adjustable elastic constants under variable compressive strain. First, the geometry configuration and samples of the proposed metamaterial are designed and fabricated at the centimetric and micrometric scales. Then, a theoretical model of the effective elastic constants is built to reveal the effects of geometrical parameters and to explain the multi-step behavior of the metamaterial. The tunable Young's modulus and auxeticity in different steps are discussed experimentally. In addition, the potential application to metamaterials with adjustable phononic band gaps is investigated numerically. Finally, the delocalized deformation mode and the reusable properties of the metamaterials are revealed.

## 2 Structural Design

In a previous work[56], inspired by the shape of latitude and longitude lines around the earth, some of us proposed and investigated a primitive motif substructure that exhibits non-auxeticity in the $x-$direction but auxeticity in the $y-$direction when either compression or stretching is applied along the $z-$direction, as depicted in Fig. 1**a**. This partially auxetic substructure consists of two different elliptical rings located in perpendicular planes, that is, in the $x-y$ plane and the $x-z$ plane.

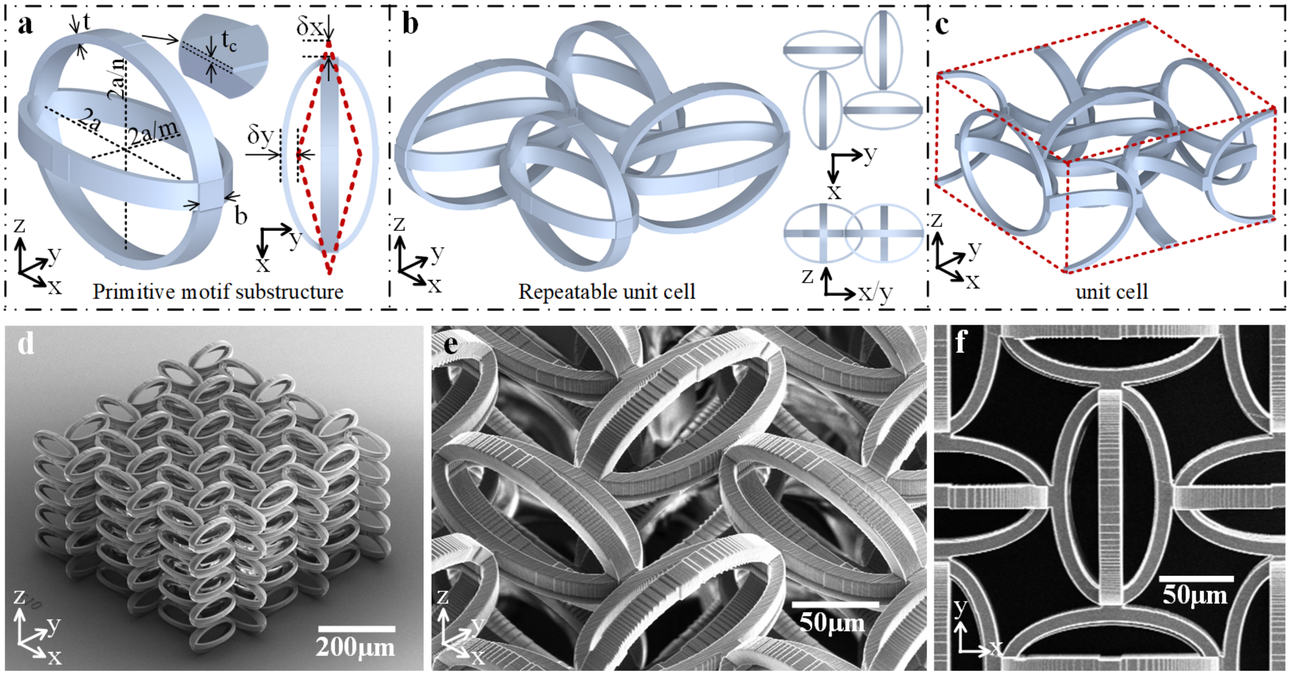

**Figure 1.** Structure design of multi-step mechanical metamaterials. **a** The primitive motif substructure shows auxeticity in the $y-$ and $z-$directions but non-auxeticity in the $x-$direction[56]. It is worth noting that for some specific geometrical parameters, i.e., $m$ and $n$ (see the text for their definition), the contraction in the $y-$direction surpasses the expansion in the $x-$direction when compression is applied in the $z-$direction, that is $\delta y > \delta x$. **b** The repeatable unit cell with auxeticity in three principal directions is obtained by alternatively arranging the partially auxetic substructure in the $x-$ and $y-$ directions. **c** The primitive unit cell is used for phononic band structure computations. We use the repeatable unit cell for experiments, rather than the primitive unit cell because the former can diminish boundary effects when the number of unit cells composing the sample is limited. **d**-**f** SEM images of a sample composed of $3 \times 3 \times 5$ unit cells fabricated with two-photon lithography. Here $m = n = 1.97$ with other parameters fixed as $a = 75\ \mu$m, $t = 10\ \mu$m, $b = 16\ \mu$m and $t_c = 0.5\ \mu$m. **d** is an oblique view of the sample, whereas **e** and **f** show zoomed-in details of the sample.

Herein, we set the geometry dimensions of the substructure in the $x-$, $y-$, and $z-$ directions as $2a$, $2a/m$, and $2a/n$, respectively. The geometry parameters $m$ and $n$ are dimensionless and independent of each other, which are used to describe the shape of the elliptical ring in the $xy-$plane and the $xz-$plane. It is clear that $m$ or $n$ equals 1 means that the ring is circular, otherwise it is elliptic. In addition, all elliptical rings of the substructure have identical cross-sections, specifically the same width $b$ and thickness $t$. Another significant geometry parameter is the distance between the outer surfaces of two adjacent elliptical rings in the $xz-$plane, $t_c$. Parameter $t_c$ has a crucial influence on the tunable effective elastic constants obtained at different compression steps and will be discussed in detail in the following sections.

The results in Ref.[56] demonstrate that the auxeticity of the substructure only depends on the geometry parameters $m$ and $n$, which means that the lateral deformation characteristics of the considered metamaterial depend on the shape of these two orthogonal elliptical rings. For some geometry parameters, significantly, an important property of this substructure is that shrinkage in the $y-$direction is larger than expansion in the $x-$ direction if the compressive loading is applied from the $z-$ direction, that is, $\delta y > \delta x$, as shown with a red dotted line in Fig. 1**a**. It is worth noting that $\delta x$ and $\delta y$ denote the absolute deformations of the substructure rather than the corresponding effective strains. Based on this inherent property, four substructures can be arranged alternatively in the $x-$ and $y-$directions to obtain a repeatable unit cell exhibiting auxeticity in all three orthogonal directions, as illustrated in Fig. 1**b**. The corresponding primitive unit cell is depicted in Fig. 1**c**.

As a note, there are three main differences between the original substructure in Fig.1**a** and the new unit cell proposed in Fig.1**c**. First, the anisotropic properties of the two unit cells are different. The original substructure exhibits anisotropy in the three principal directions, whereas the new unit cell has identical mechanical properties in both $x-$ and $y-$ directions because of symmetry. Second, the original substructure is non-auxetic in one principal direction but auxetic in the other two principal directions. In contrast, the new unit cell is fully auxetic in all three principal directions. Third, elastically-stable multi-step mechanical behavior is hardly achieved by the original substructure, as it avoids self-contacts under large compression. The elastically-stable multi-step mechanical behavior resulting from self-contact is the distinctive property of the proposed metamaterial and is discussed in detail in this work.

## 3 Materials and Methods

### 3.1 Fabrication

A commercial 3D printer (Photonic Professional GT+, Nanoscrible GmbH, Germany) based on the principles of two-photon lithography 3D direct laser writing technology was used to prepare micro-scale metamaterials, as shown in Fig. 1**d**-**f**. The parent material for these samples is the customized commercial negative tone IP-S resin. Young's modulus, Poisson's ratio, and density for the raw resin material are $E = 4$ GPa, $\nu = 0.3$, and $\rho = 1190$ kg/m$^3$, respectively. For the Nanoscribe printing, the slicing distance and the hatching distance are prescribed to 1 $\mu$m and 0.5 $\mu$m, respectively. A drop of IP-S resin was deposited on an ITO-coated soda-lime glass substrate with dimensions 25 mm × 25 mm × 0.7 mm and photopolymerized with a femtosecond laser operating at $\lambda = 780$ nm and a $25\times-$ objective. The sample comprises $3 \times 3 \times 5$ unit cells (see Fig. 1**d**) in the main directions, and each repeatable unit cell (see Fig. 1**b**) was printed layer by layer from bottom to top. After printing, the samples were developed for 30 min in a propylene glycol methyl ether acetate (PGMEA) solution to remove the unexposed photoresist and were rinsed for 5 min in isopropyl alcohol (IPA) to clear the developer. Laser power at the level of 90 percent and a galvanometric scan speed of 100 mm/s were used for the whole fabrication process.

The centimetric samples (see Fig. 6**a**) were fabricated by a commercial 3D printing company (Mohou Ltd, Beijing, China) with a selective laser sintering 3D printing craft. Thermoplastic urethane (TPU) with white color was used as the raw material. Young's modulus, Poisson's ratio, density, and the elongation of the raw material TPU are 27 MPa, 0.45, 1200 kg/m$^3$ and 500%, respectively.

### 3.2 Mechanical Tests

To evaluate the static mechanical properties of the metamaterials, quasi-static uniaxially compressive experiments were performed. 5 samples were prepared at the micro-scale and were tested with a homemade setup with a load capacity of 5 N, a resolution of $10^{-6}$ N, and a compression speed set to 1 $\mu$m/s. At the same time, a microscope (LV-UEP, Nikon, Japan) equipped with a lens (566039, Leica, Germany) of 20× magnification and the recording rate of 1 frame per second was used to capture the deformation of the sample in time. A video for the whole compressive process was exported. More specifically, the image tracking functions from MATLAB software were employed to process and extract lateral deformations of the micro-scale samples. In terms of macroscopic testing, the 5 cycles of the loading and unloading experiments for each sample on a centimeter scale were implemented in an INSTRON 5569 mechanical tester with a load cell capacity of 50 kN. The compressive speed was fixed at 1 mm/s to maintain the quasistatic deformation and avoid dynamic effects. At the same time, commercial digital image correlation (DIC, Correlated Solutions, Inc.) equipment was used to record lateral deformations along the course. The applied DIC device measures arbitrary displacements down to nanometer resolution. Here, strain measurements from 50 microstrain to 2500% and above are available with 10-50 microstrain or better strain resolution. The device allows to assess specimen sizes ranging from 1 mm to 100 mm as well as to capture dynamic events at the rate of 5000000 frames per second. Images were processed by matching software VIC-3D, where a contour representing the displacement in the $x$-direction was output directly, as shown in Fig. 6**g**.

## 3.3 Analytical Model

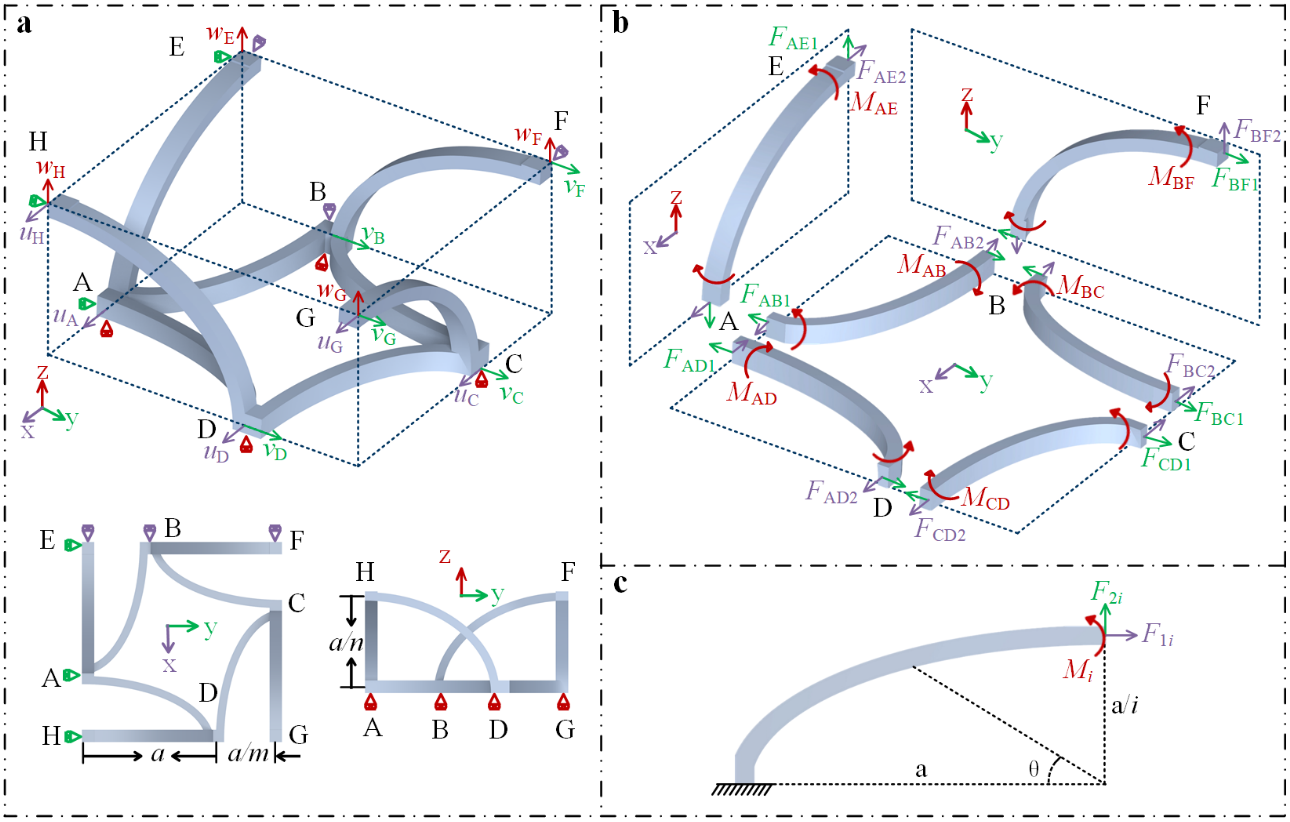

**Figure 2.** Force analysis of mechanical metamaterials under loading in the $z-$direction and periodic boundary conditions. **a** Force analysis of a $1/8$-th representative volume element of the proposed metamaterial. **b** Decomposition of the $1/8$-th representative volume element. **c** Force analysis for each single beam.

To obtain the effective mechanical properties of the metamaterial, a theoretical model was built based on the force method of continuum mechanics. The following assumptions were made. First, we used the unit cell shown in Fig. 1**c** as the representative volume element for the metamaterial, and periodic boundary conditions were applied in all three principal directions. Second, the situation that the structure is under small compressive/stretch deformation in the $z-$ direction is taken into consideration merely. Then, all joints in the structure are assumed to be rigid. Moreover, the axial and shear deformations are neglected so it can be assumed that all members in the proposed structure are Euler beams that are deforming by bending only[57].

Herein, we assume that a stretch (or a compressive) pre-displacement is applied in the $z-$ direction on the representative volume element. As declared above, it is clear that the mechanical properties of the structure in the $x-$ and $y-$ directions are identical. Due to the symmetry of the structure in the three principal directions, the loading and corresponding boundary conditions of a $1/8$-th representative volume element are considered and analyzed, as shown in Fig. 2**a**. For the considered $1/8$ unit cell, it is clear that the degrees of freedom of plane BEF in the $x-$ direction, plane AEH in the $y-$ direction, and plane ABCD in the $z-$ direction are fixed. However, the other three faces parallel to them can move in the corresponding directions. Furthermore, we can decompose the $1/8$-th representative volume element at each joint and obtain the force conditions of each beam[58], as illustrated in Fig. 2**b**.

For each member of the $1/8$-th representative volume element, the effective loading and boundary conditions are identical, as shown in Fig. 2**c**. We assume that forces $F_{1i} = F_{2i} = 1$ N and moments $M_i = 1$ N.m, for $i = m, n$, so that we can obtain the following parameters[57] by the force method of continuum mechanics,

$$\begin{cases} \delta_{F_{1i}F_{1i}} = \frac{a^3}{EI}\int_0^{\pi/2}\left(\frac{1}{i}-\frac{\sin\theta}{\sqrt{i^2\sin^2\theta+\cos^2\theta}}\right)^2\frac{1}{\sqrt{i^2\sin^2\theta+\cos^2\theta}}d\theta, \\ \delta_{F_{1i}F_{2i}} = -\frac{a^3}{EI}\int_0^{\pi/2}\left(\frac{1}{i}-\frac{\sin\theta}{\sqrt{i^2\sin^2\theta+\cos^2\theta}}\right)\frac{\cos\theta}{i^2\sin^2\theta+\cos^2\theta}d\theta, \\ \delta_{F_{2i}F_{2i}} = \frac{a^3}{EI}\int_0^{\pi/2}\frac{\cos^2\theta}{\sqrt{i^2\sin^2\theta+\cos^2\theta}^3}d\theta, \\ \delta_{M_iM_i} = \frac{a}{EI}\int_0^{\pi/2}\frac{1}{\sqrt{i^2\sin^2\theta+\cos^2\theta}}d\theta, \\ \delta_{F_{2i}M_i} = \frac{a^2}{EI}\int_0^{\pi/2}\frac{\cos\theta}{i^2\sin^2\theta+\cos^2\theta}d\theta, \\ \delta_{F_{1i}M_i} = -\frac{a^2}{EI}\int_0^{\pi/2}\left(\frac{1}{i}-\frac{\sin\theta}{\sqrt{i^2\sin^2\theta+\cos^2\theta}}\right)\frac{1}{\sqrt{i^2\sin^2\theta+\cos^2\theta}}d\theta, \end{cases} \tag{1}$$

where $\delta_{jk} = \delta_{kj}$ is the displacement component in $j-$direction introduced by the unit force in the $k-$direction, and $E$ and $I = \frac{bt^3}{24}$ represent Young's modulus of the raw material and the moment of inertia of the beam, respectively.

For beam AB, we can use the following equations to calculate the displacements in the $F_{\mathrm{AB1}}$, the $F_{\mathrm{AB2}}$ and the $M_{\mathrm{AB}}$ directions, respectively,

$$\begin{bmatrix} \delta_{F_{\mathrm{AB2}}F_{\mathrm{AB1}}} & \delta_{F_{\mathrm{AB2}}F_{\mathrm{AB2}}} & \delta_{F_{\mathrm{AB2}}M_{\mathrm{AB}}} \\ \delta_{F_{\mathrm{AB1}}F_{\mathrm{AB1}}} & \delta_{F_{\mathrm{AB1}}F_{\mathrm{AB2}}} & \delta_{F_{\mathrm{AB1}}M_{\mathrm{AB}}} \\ \delta_{M_{\mathrm{AB}}F_{\mathrm{AB1}}} & \delta_{M_{\mathrm{AB}}F_{\mathrm{AB2}}} & \delta_{M_{\mathrm{AB}}M_{\mathrm{AB}}} \end{bmatrix} \begin{bmatrix} F_{\mathrm{AB1}} \\ F_{\mathrm{AB2}} \\ M_{\mathrm{AB}} \end{bmatrix} = \begin{bmatrix} u_{\mathrm{A}} \\ v_{\mathrm{B}} \\ 0 \end{bmatrix}. \tag{2}$$

Similarly, for beam AD,

$$\begin{bmatrix} \delta_{F_{\mathrm{AD2}}F_{\mathrm{AD1}}} & \delta_{F_{\mathrm{AD2}}F_{\mathrm{AD2}}} & \delta_{F_{\mathrm{AD2}}M_{\mathrm{AD}}} \\ \delta_{F_{\mathrm{AD1}}F_{\mathrm{AD1}}} & \delta_{F_{\mathrm{AD1}}F_{\mathrm{AD2}}} & \delta_{F_{\mathrm{AD1}}M_{\mathrm{AD}}} \\ \delta_{M_{\mathrm{AD}}F_{\mathrm{AD1}}} & \delta_{M_{\mathrm{AD}}F_{\mathrm{AD2}}} & \delta_{M_{\mathrm{AD}}M_{\mathrm{AD}}} \end{bmatrix} \begin{bmatrix} F_{\mathrm{AD1}} \\ F_{\mathrm{AD2}} \\ M_{\mathrm{AD}} \end{bmatrix} = \begin{bmatrix} u_{\mathrm{D}} - u_{\mathrm{A}} \\ v_{\mathrm{D}} \\ 0 \end{bmatrix}. \tag{3}$$

For beam BC,

$$\begin{bmatrix} \delta_{F_{\mathrm{BC2}}F_{\mathrm{BC1}}} & \delta_{F_{\mathrm{BC2}}F_{\mathrm{BC2}}} & \delta_{F_{\mathrm{BC2}}M_{\mathrm{BC}}} \\ \delta_{F_{\mathrm{BC1}}F_{\mathrm{BC1}}} & \delta_{F_{\mathrm{BC1}}F_{\mathrm{BC2}}} & \delta_{F_{\mathrm{BC1}}M_{\mathrm{BC}}} \\ \delta_{M_{\mathrm{BC}}F_{\mathrm{BC1}}} & \delta_{M_{\mathrm{BC}}F_{\mathrm{BC2}}} & \delta_{M_{\mathrm{BC}}M_{\mathrm{BC}}} \end{bmatrix} \begin{bmatrix} F_{\mathrm{BC1}} \\ F_{\mathrm{BC2}} \\ M_{\mathrm{BC}} \end{bmatrix} = \begin{bmatrix} u_{\mathrm{C}} \\ v_{\mathrm{C}} - v_{\mathrm{B}} \\ 0 \end{bmatrix}. \tag{4}$$

For beam CD,

$$\begin{bmatrix} \delta_{F_{\mathrm{CD2}}F_{\mathrm{CD1}}} & \delta_{F_{\mathrm{CD2}}F_{\mathrm{CD2}}} & \delta_{F_{\mathrm{CD2}}M_{\mathrm{CD}}} \\ \delta_{F_{\mathrm{CD1}}F_{\mathrm{CD1}}} & \delta_{F_{\mathrm{CD1}}F_{\mathrm{CD2}}} & \delta_{F_{\mathrm{CD1}}M_{\mathrm{CD}}} \\ \delta_{M_{\mathrm{CD}}F_{\mathrm{CD1}}} & \delta_{M_{\mathrm{CD}}F_{\mathrm{CD2}}} & \delta_{M_{\mathrm{CD}}M_{\mathrm{CD}}} \end{bmatrix} \begin{bmatrix} F_{\mathrm{CD1}} \\ F_{\mathrm{CD2}} \\ M_{\mathrm{CD}} \end{bmatrix} = \begin{bmatrix} u_{\mathrm{D}} - u_{\mathrm{C}} \\ v_{\mathrm{C}} - v_{\mathrm{D}} \\ 0 \end{bmatrix}. \tag{5}$$

For beam AE,

$$\begin{bmatrix} \delta_{F_{\mathrm{AE2}}F_{\mathrm{AE1}}} & \delta_{F_{\mathrm{AE2}}F_{\mathrm{AE2}}} & \delta_{F_{\mathrm{AE2}}M_{\mathrm{AE}}} \\ \delta_{F_{\mathrm{AE1}}F_{\mathrm{AE1}}} & \delta_{F_{\mathrm{AE1}}F_{\mathrm{AE2}}} & \delta_{F_{\mathrm{AE1}}M_{\mathrm{AE}}} \\ \delta_{M_{\mathrm{AE}}F_{\mathrm{AE1}}} & \delta_{M_{\mathrm{AE}}F_{\mathrm{AE2}}} & \delta_{M_{\mathrm{AE}}M_{\mathrm{AE}}} \end{bmatrix} \begin{bmatrix} F_{\mathrm{AE1}} \\ F_{\mathrm{AE2}} \\ M_{\mathrm{AE}} \end{bmatrix} = \begin{bmatrix} u_{\mathrm{A}} \\ w_{\mathrm{E}} \\ 0 \end{bmatrix}. \tag{6}$$

For beam BF,

$$\begin{bmatrix} \delta_{F_{\mathrm{BF1}}F_{\mathrm{BF1}}} & \delta_{F_{\mathrm{BF1}}F_{\mathrm{BF2}}} & \delta_{F_{\mathrm{BF1}}M_{\mathrm{BF}}} \\ \delta_{F_{\mathrm{BF2}}F_{\mathrm{BF1}}} & \delta_{F_{\mathrm{BF2}}F_{\mathrm{BF2}}} & \delta_{F_{\mathrm{BF2}}M_{\mathrm{BF}}} \\ \delta_{M_{\mathrm{BF}}F_{\mathrm{BF1}}} & \delta_{M_{\mathrm{BF}}F_{\mathrm{BF2}}} & \delta_{M_{\mathrm{BF}}M_{\mathrm{BF}}} \end{bmatrix} \begin{bmatrix} F_{\mathrm{BF1}} \\ F_{\mathrm{BF2}} \\ M_{\mathrm{BF}} \end{bmatrix} = \begin{bmatrix} v_{\mathrm{F}} - v_{\mathrm{B}} \\ w_{\mathrm{F}} \\ 0 \end{bmatrix}, \tag{7}$$

where

$$\begin{cases} \delta_{F_{\mathrm{AB2}}F_{\mathrm{AB2}}} = \delta_{F_{\mathrm{AD1}}F_{\mathrm{AD1}}} = \delta_{F_{\mathrm{BC1}}F_{\mathrm{BC1}}} = \delta_{F_{\mathrm{CD2}}F_{\mathrm{CD2}}} = \delta_{F_{1i}F_{1i}}, \\ \delta_{F_{\mathrm{AB1}}F_{\mathrm{AB1}}} = \delta_{F_{\mathrm{AD2}}F_{\mathrm{AD2}}} = \delta_{F_{\mathrm{BC2}}F_{\mathrm{BC2}}} = \delta_{F_{\mathrm{CD1}}F_{\mathrm{CD1}}} = \delta_{F_{2i}F_{2i}}, \\ \delta_{F_{\mathrm{AB1}}F_{\mathrm{AB2}}} = \delta_{F_{\mathrm{AD1}}F_{\mathrm{AD2}}} = \delta_{F_{\mathrm{BC1}}F_{\mathrm{BC2}}} = \delta_{F_{\mathrm{CD1}}F_{\mathrm{CD2}}} = \delta_{F_{1i}F_{2i}}, \\ \delta_{F_{\mathrm{AB1}}M_{\mathrm{AB}}} = \delta_{F_{\mathrm{AD2}}M_{\mathrm{AD}}} = \delta_{F_{\mathrm{BC2}}M_{\mathrm{BC}}} = \delta_{F_{\mathrm{CD1}}M_{\mathrm{CD}}} = \delta_{F_{2i}M_i}, \\ \delta_{F_{\mathrm{AB2}}M_{\mathrm{AB}}} = \delta_{F_{\mathrm{AD1}}M_{\mathrm{AD}}} = \delta_{F_{\mathrm{BC1}}M_{\mathrm{BC}}} = \delta_{F_{\mathrm{CD2}}M_{\mathrm{CD}}} = \delta_{F_{1i}M_i}, \\ \delta_{M_{\mathrm{AB}}M_{\mathrm{AB}}} = \delta_{M_{\mathrm{AD}}M_{\mathrm{AD}}} = \delta_{M_{\mathrm{BC}}M_{\mathrm{BC}}} = \delta_{M_{\mathrm{CD}}M_{\mathrm{CD}}} = \delta_{M_iM_i}, \end{cases} \tag{8}$$

for $i = m$ and

$$\begin{cases} \delta_{F_{\mathrm{AE2}}F_{\mathrm{AE2}}} = \delta_{F_{\mathrm{BF1}}F_{\mathrm{BF1}}} = \delta_{F_{1i}F_{1i}}, \\ \delta_{F_{\mathrm{AE1}}F_{\mathrm{AE1}}} = \delta_{F_{\mathrm{BF2}}F_{\mathrm{BF2}}} = \delta_{F_{2i}F_{2i}}, \\ \delta_{F_{\mathrm{AE2}}F_{\mathrm{AE1}}} = \delta_{F_{\mathrm{BF1}}F_{\mathrm{BF2}}} = \delta_{F_{1i}F_{2i}}, \\ \delta_{F_{\mathrm{AE1}}M_{\mathrm{AE}}} = \delta_{F_{\mathrm{BF2}}M_{\mathrm{BF}}} = \delta_{F_{2i}M_i}, \\ \delta_{F_{\mathrm{AE2}}M_{\mathrm{AE}}} = \delta_{F_{\mathrm{BF1}}M_{\mathrm{BF}}} = \delta_{F_{1i}M_i}, \\ \delta_{M_{\mathrm{AE}}M_{\mathrm{AE}}} = \delta_{M_{\mathrm{BF}}M_{\mathrm{BF}}} = \delta_{M_iM_i}, \end{cases} \tag{9}$$

for $i = n$.

The physical meaning of the third row of each matrix is that the rotational angle at each endpoint is 0.

Based on the periodicity and the symmetry of the structure, the displacement-matching conditions at each endpoint can be acquired[48],

$$\begin{cases} u_{\mathrm{D}} = u_{\mathrm{G}} = u_{\mathrm{H}}, \\ v_{\mathrm{C}} = v_{\mathrm{F}} = v_{\mathrm{G}}, \\ w_{\mathrm{E}} = w_{\mathrm{F}} = w_{\mathrm{G}} = w_{\mathrm{H}}, \\ u_{\mathrm{A}} = u_{\mathrm{G}} - u_{\mathrm{C}}, \\ v_{\mathrm{B}} = v_{\mathrm{G}} - v_{\mathrm{D}}. \end{cases} \tag{10}$$

During the quasi-static loading, the force equilibrium conditions are always suitable for each endpoint. Based on the force balance at point A in the $x-$direction, we have

$$F_{\mathrm{AB2}} + F_{\mathrm{AE2}} - F_{\mathrm{AD2}} = 0. \tag{11}$$

and the force equilibrium is also satisfied at point B in $y$ direction,

$$F_{\mathrm{AB1}} - F_{\mathrm{BC1}} - F_{\mathrm{BF1}} = 0. \tag{12}$$

Due to all degrees of freedom of plane CFG in the $y-$direction being free, the total force along the $y-$direction in this surface should be 0, that is,

$$F_{\mathrm{BF1}} + F_{\mathrm{BC1}} + F_{\mathrm{CD1}} = 0. \tag{13}$$

Similarly, we have the same force conditions for plane DGH in the $x-$direction,

$$F_{\mathrm{AE2}} + F_{\mathrm{AD2}} + F_{\mathrm{CD2}} = 0. \tag{14}$$

Moreover, the relationship between effective stress and effective strain in the $z-$ direction is

$$2(F_{\mathrm{AE1}} + F_{\mathrm{BF2}}) = \sigma_z \left(a + \frac{a}{m} + t\right)^2. \tag{15}$$

So, the effective strain of the structure in the $x-$ and the $z-$directions can be calculated as

$$\begin{cases} \varepsilon_x = \dfrac{u_{\mathrm{D}}}{a + \frac{a}{m} + t}, \\ \varepsilon_z = \dfrac{w_{\mathrm{E}}}{\frac{a}{n} + \frac{t}{2}}. \end{cases} \tag{16}$$

Finally, the effective elastic constants, i.e., the effective Poisson's ratio and normalized Young's modulus, of the proposed metamaterial can be obtained,

$$\begin{cases} \nu_{zx} = -\frac{\varepsilon_x}{\varepsilon_z}, \\ \hat{E}_{zn} = \frac{\sigma_z}{E\varepsilon_z}. \end{cases} \tag{17}$$

### 3.4 Simulations

Numerical calculations were performed using the commercial software COMSOL Multiphysics 6.0 with the Structural Mechanics module. First of all, the CAD model of the unit cell (see Fig. 1**c**) was built in software CATIA V5R20, then the model was imported in COMSOL Multiphysics 6.0. It was assumed that the material that the unit cell is made of has the same properties as the bulk material used during the fabrication process. Thus, the isotropic material assigned to the model was characterized by Young's modulus of 4 GPa, Poisson's ratio equal to 0.3, and density set to be 1190 kg/m$^3$. To explore the structural nonlinearity of the unit cell under large deformations, elastoplasticity of the raw material was ignored in this simulation. In addition, periodic boundary conditions were applied to all three principal directions. It is worth noting that all boundary surfaces of the unit cell remain planar after deformation since only a metamaterial under longitudinal compression is taken into account in this work. The same boundary conditions are applied to the theoretical model, as discussed in the previous subsection. For the static compression simulations, the periodicity is set as

$$\begin{bmatrix} u_{\mathrm{dst}} \\ v_{\mathrm{dst}} \\ w_{\mathrm{dst}} \end{bmatrix} = \begin{bmatrix} i & j & k \end{bmatrix} \begin{bmatrix} u_{\mathrm{src}} \\ v_{\mathrm{src}} \\ w_{\mathrm{src}} \end{bmatrix}, \tag{18}$$

where "dst" is the destination and "src" is the source. If the plane is perpendicular to the $x$ direction, $i = -1$ and $j = k = 1$. If the plane is perpendicular to the $y$ or $z$ directions, similar rules apply, i.e., $j = -1$, $i = k = 1$ and $k = -1$, $i = j = 1$ respectively. For the computation of dispersion relations, Floquet-Bloch periodicity was applied to the primitive unit cell. The first Brillouin zone of the unit cell is shown as an insert in Fig. 5**a**[59]. For elliptical rings in the $xz$ and $yz$ planes, the "contact pair" is defined between their outer surface and their neighbor in the $z-$direction. The augmented Lagrangian method and equations were used to describe the contact properties. The entire structure is meshed by approximately 30000 free tetrahedral elements. Finally, the prestressed-eigenfrequency module is used to obtain the dispersion relation. More specifically, the computation process in divided in two steps. In the first step, the stationary module is employed to apply a prescribed displacement to the metamaterial in the $z-$direction. For instance, in the case of the unit cell with a 20 $\mu$m prescribed displacement, displacements of $-10$ $\mu$m and 10 $\mu$m are imposed to the top and bottom boundary surfaces of the unit cell along the $z-$direction. In the second step, the eigenfrequency module is used to calculate the dispersion relation. It is worth noting that the computation in the second step depends on the results from the first step, since stresses are introduced in each curved beam. Hence, the prescribed deformations and the dispersion relations of the considered metamaterial must be computed step by step.

## 4 Results and Discussions

### 4.1 Effective Mechanical Properties of the Proposed Metamaterials

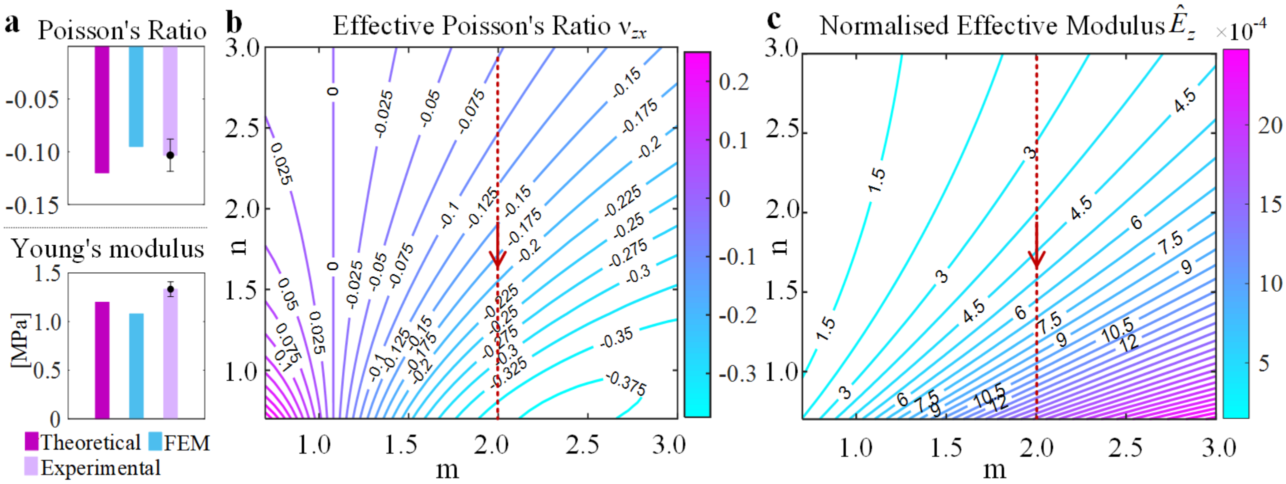

**Figure 3.** Effective Young's Modulus and Auxeticity of the proposed metamaterials. **a** Effective elastic constants of the metamaterial under small deformations obtained by different methods are compared. **b** The trend in the effective Poisson's ratio is shown as a function of the change in $m$ and $n$. **c** The variation of the normalized effective modulus versus the geometric parameters. other parameters set as $a = 75$ $\mu$m, $t = 10$ $\mu$m, $b = 16$ $\mu$m and $t_c = 0.5$ $\mu$m.

To explore the influence of the shape of each elliptical ring, described by parameters $m$ and $n$, on effective elastic constants, a theoretical model was built based on the theory of beams[57,58] (see Materials and Methods Section). Effective elastic constants of the metamaterial under small deformations obtained by different methods are compared in Fig. 3**a**. As a note, the effective elastic constants under small deformation in experimental and numerical results are calculated from the slope of the curves for compressive strain ranging from 0 to 0.05. This method is different from the method used in the following subsection to compute the elastic constants at different steps, since in the latter case the metamaterial is significantly deformed. The results shown in Fig. 3**a** validate the theoretical model built in this work, as the results obtained by these three methods match well. The variations predicted by the theoretical model of the effective Poisson's ratio and the normalized effective modulus of the metamaterial with $m$ and $n$ varying in the range from 0.7 to 3 are shown in Fig. 3**b** and Fig. 3**c**. In general, both $m$ and $n$ significantly impact the effective constants.

The following points are highlighted. First, only the shape of the elliptical ring in the $xy-$plane, controlled by parameter $m$, determines the auxeticity of the entire structure, i.e., the sign of the effective Poisson's ratio. As demonstrated by Fig. 3**b**, if $m$ is smaller than 1.1 the metamaterial is non-auxetic, and if $m > 1.1$ it is auxetic. Hence, the shape of the elliptical ring in the $xz-$plane, controlled by parameter $n$, does not influence the sign of the effective Poisson's ratio. This deformation property is the reason for the metamaterial undergoes an elastically-stable continuous phase transition of the Poisson's ratio, as we reported in another work[48]. Second, when parameters $m$ and $n$ are in the range $[0.7, 3]$, their influences on the normalized effective modulus are opposite. An increasing value for $m$ and $n$ means a decrease in the aspect ratio of the curved beam in each elliptical ring. In other words, the curved beam tends toward a straight beam with increasing $m$ and $n$. The curved beam in the $xy$-plane with a smaller aspect ratio (larger $m$) enhances the constraint of deformation of the whole structure and increases the modulus of the system. Conversely, the smaller aspect ratio of the curved beam in the $xz$-plane (larger $n$) has a negative influence on the force transmission in the $z$-direction and thus decreases the modulus of the system. These are fundamental reasons why parameters $m$ and $n$ have opposite effects on the normalized effective modulus.

More importantly, the theoretical predictions imply that both auxeticity and effective Young's modulus of the metamaterial will be enhanced with the lessening of parameter $n$ if the value of parameter $m$ is close to 2, as demonstrated in dark red dotted lines and arrows in Fig. 3. In other words, it is possible to magnify the aspect ratio (corresponding to the reducing of parameter $n$) of the elliptical rings in the $xz-$ and $yz-$ plane to cement the elastic properties of the metamaterial when the shape of elliptical rings in the $xy-$ plane remains constant. This point can provide fundamental insights into the multi-step behavior of the metamaterial which will be discussed in detail in the following subsections.

### 4.2 Multi-step Behavior and Tunable Elastic Constants

This subsection focuses on the experimental and numerical investigation of the multi-step behavior and tunable mechanical properties of the designed metamaterial under large compressive deformation. The samples studied in this subsection are fabricated by the two-photon lithography 3D printing (see Materials and Methods section) technology with IP-S resin (with Young's modulus 4.0 GPa, Poisson's ratio 0.3 and density 1.19 g/cm$^3$), as illustrated in Fig. 1**d**-**f**. The geometrical parameters of the samples have been set as $m = n = 1.97$, $a = 75$ $\mu$m, $t = 10$ $\mu$m, $b = 16$ $\mu$m and $t_c = 0.5$ $\mu$m, respectively.

Experimental and numerical results are presented in Fig. 4. In both experimental and numerical results, the reaction force divided by the cross-section of the samples and the deformation between top and bottom boundary surfaces divided by the size of the samples in the $z$-direction were used respectively to compute the effective stress ($\sigma_z$ ) and effective strain ($\varepsilon_z$). The lateral deformation in the central region of the sample is divided by the original size of this region to calculate the effective lateral strain ($\varepsilon_x$). The experimental effective elastic constants, i.e., lateral strain $\varepsilon_x$ and compression stress $\sigma_z$ versus compressive strain $\varepsilon_z$, are shown in Fig. 4**a**-**d**. Herein, we resolve the whole compression process into two main steps, called Step-1 and Step-2. As can be seen in Fig. 4, the lateral strain $\varepsilon_x$ and the compressive stress $\sigma_z$ exhibit completely different trends in either step. In order to ascribe effective elastic constants to the metamaterial at each step, the slope of the lateral strain versus vertical strain and the counterpart of the compressive stress versus compressive strain at each step were used to figure out the corresponding effective Poisson's ratio and Young's modulus. With this definition, the effective elastic constants for each step are reported in Fig. 4**b** and **d**. It is clear that both the effective Poisson's ratio $\nu_{zx}$ and Young's modulus $E_z$ of the metamaterial are enhanced when the compression process jumps from Step-1 to Step-2. $\nu_{zx} = -0.12$ and $E_z = 1.2$ MPa for the first step, and $\nu_{zx} = -0.3$ and $E_z = 2.6$ MPa for the second step. Significantly, the numerical results obtained with FEM confirm the variations of the elastic constants, as Fig. 4**h** shows.

To reveal the nature of variations of the elastic constants in either step, experimental and numerical compressive deformations are reported in Fig. 4**e** and **f**, respectively. It is worth noting that the outer surface of the curved beams which are in the $xz-$ and $yz-$planes contact the counterparts of their neighbors in the $z-$ direction if the compression strain reaches a critical value, equal to 30% in experiments and to 26% in simulations. This self-contact is the key element that enhances the elastic constants and marks the separation between steps due to the resulting modification of the effective geometrical parameter of the unit cell. As a matter of fact, after contact the effective aspect ratios of the curved beams in the $xz$- and $yz$-planes increase, as highlighted by the green curves in Fig. 4**f**. This increase in the aspect ratio of curved beams enhances the force transmission in the $z$-direction. The aspect ratio of the curved beam in the $xy$-plane, however, remains unchanged at the critical strain (the strain at the onset of contact) for Step-1 and Step-2. Hence, the contact alters the shape of the curved beams in the vertical direction but does not modify the configuration of the curved beam in the horizontal direction, as demonstrated in Fig. 4**f**. More specifically, the effective value of $n$ decreases whereas $m$ remains unchanged, so that the geometric parameters of the unit cell jump directly

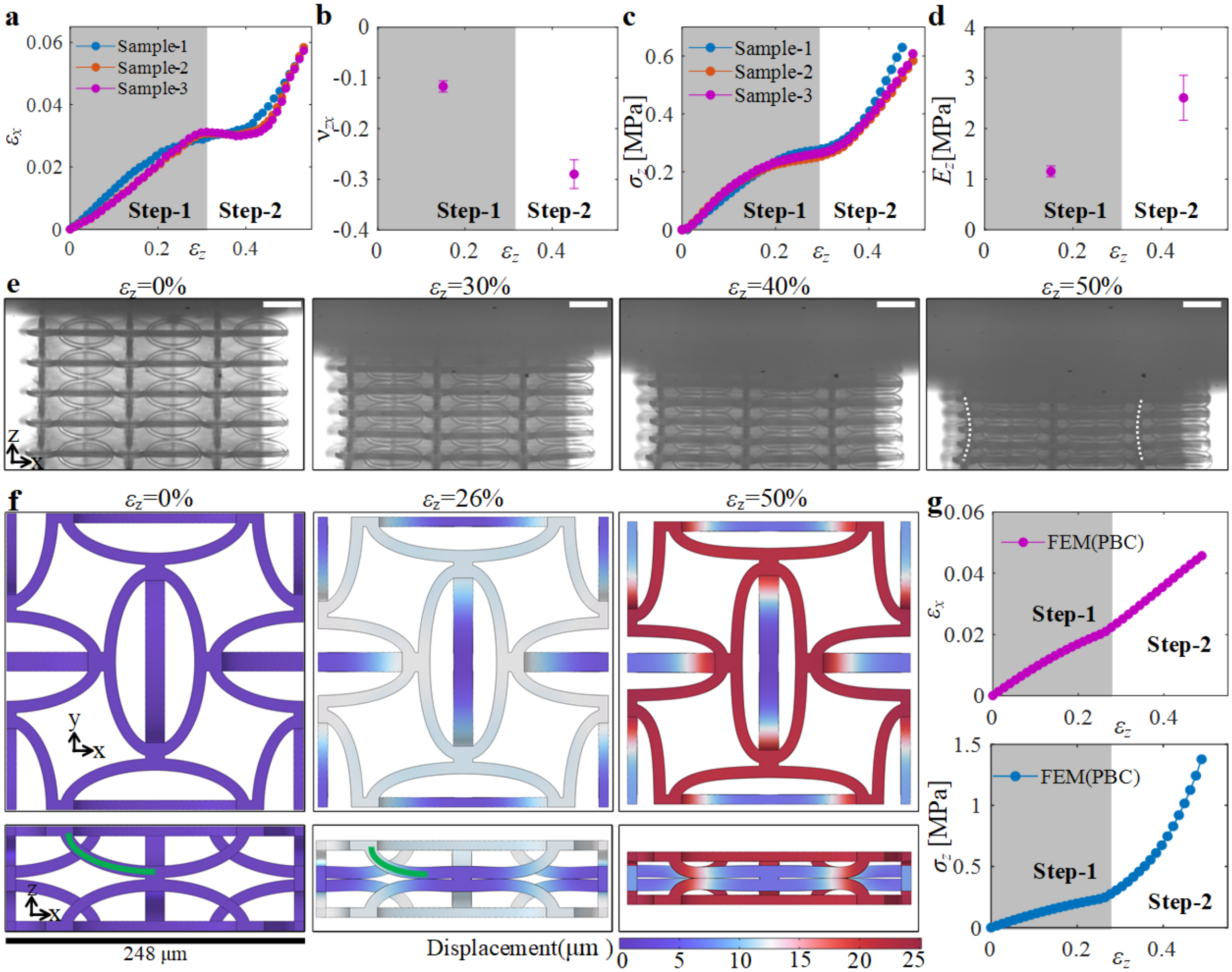

**Figure 4.** Multi-step behavior and tunable elastic constants during the compression along the $z-$direction. **a** Normalized strain $\varepsilon_x$ versus normalized strain $\varepsilon_z$. **b** Effective Poisson's ratio for Step-1 and Step-2. **c** Normalized stress $\sigma_z$ versus normalized strain $\varepsilon_z$. **d** Effective Young's modulus for both steps. **e** Experimental compression deformation (the scale bar length is 100 $\mu$m). **f** Numerical compressive deformation process of the conventional unit cell under periodic boundary conditions (PBC) applied in all three main directions. The contour plot shows the magnitude of the displacement. **g** Normalized strain $\varepsilon_x$ and normalized stress $\sigma_z$ versus $\varepsilon_z$ obtained by the finite element method (FEM).

from one point to another along the arrow direction with the red dotted line in Fig. 3**b** and **c**. As a result, both auxeticity and Young's modulus are enhanced, in good agreement with the prediction of the theoretical model in Fig. 3**b** and **c**, as discussed in the last paragraph in the previous subsection. It is worth noting that the theoretical prediction of the elastic constants assumes small deformations. They can hardly, in principle, quantify the variation of the elastic constants of the metamaterial after contact. Nevertheless, they still provide a qualitative trend. Another essential point is that the whole system remains elastically stable during the entire compression process, i.e., during both Step-1 and Step-2, without any instability of the structure or post-buckling of the raw material[48].

There are some differences between experimental and numerical results. For instance, in both experimental $\varepsilon_x(\varepsilon_z)$ and $\sigma_z(\varepsilon_z)$ curves, short plateaus can be observed. In contrast, they do not appear in the simulation results, since the elastoplasticity of the raw material is ignored in the computational model. Simulation results merely show the geometric nonlinearity of the structure, but experimental results further include the geometric and material nonlinearity of the structure and the raw material. This is one of the reasons why Young's modulus for Step-2 in experiments is smaller than in simulation. Additionally, the experimental samples are composed of a limited number of unit cells, so boundary effects can not be absolutely eliminated. More importantly, friction between the top and bottom surfaces of the samples and the mechanical testing machine limits the lateral contraction of these surfaces. In this case, the samples are deformed like a re-entrant structure during the compression process, that is the area of the cross-section of the central surface is smaller than the counterparts of the top and bottom surfaces, as shown with the white dashed line in Fig. 4**e**. This re-entrant deformation further enhances the auxeticity of the metamaterial in the experimental tests. Conversely, the simulation model assumes periodic boundary conditions in all three principal directions so that no re-entrant deformation of the unit cell can be observed during the entire compression process, as shown in Fig. 4**f**. This is the main reason why the experimental auxeticity for Step-2 surpasses the numerical auxeticity. Anyway, the predictions of the theoretical model and the experimental and simulation results all imply the same trends for the multi-step mechanical behaviors of the considered metamaterials.

### 4.3 Potential Application to Tunable Phononic Band Gap Structures

As discussed in the previous subsections, the proposed metamaterial shows different elastic constants depending on the compression strain, as if there were two different materials. Here, we want to highlight a potential application to tunable phononic band gap structures. It may not be immediately apparent, but a varying Poisson's ratio causes a modulation of the volume and hence of the relative density of porous structures and materials since the overall mass is conserved. This effect is especially strong under large compressive or stretching strain. Furthermore, Young's modulus also varies a lot with the applied strain, as we discussed above. As a result, both the relative density and the modulus, but also all effective elastic constants of the metamaterial vary with the applied strain. As a matter of fact, the dispersion of acoustic and elastic waves is highly dependent on the density and the modulus of materials[60–62].

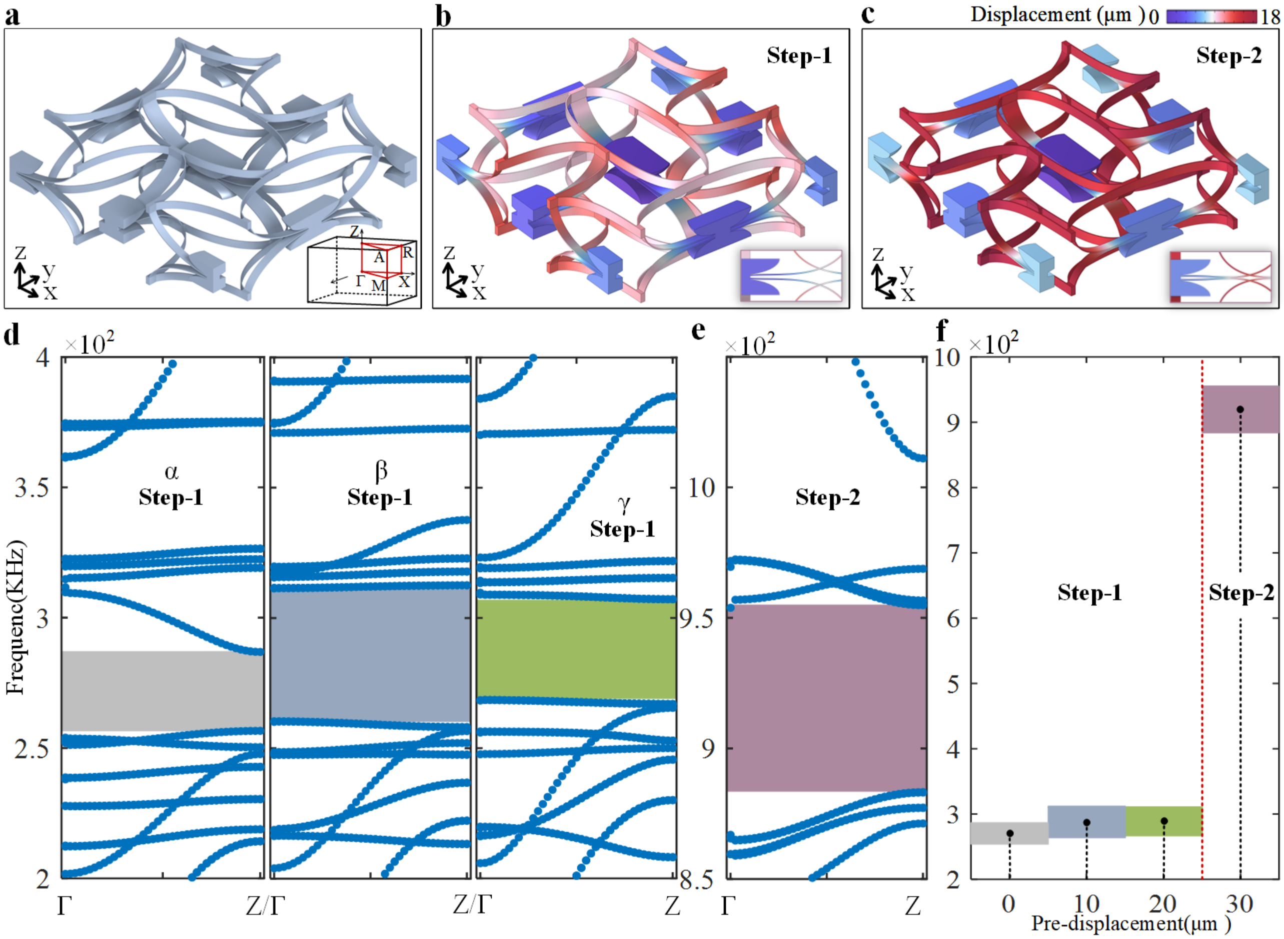

**Figure 5.** Potential application to the design of structures with a tunable phononic band gap. **a** A physical concentrated mass is added at the connecting node of the curved beams. The geometry parameters are set as $a = 79.5\ \mu$m, $t = 1\ \mu$m, $b = 16\ \mu$m, $t_c = 0.5\ \mu$m, and $m = n = 1.87$. **b** The structure undergoes a pre-displacement of 20 $\mu$m in Step-1. **c** The structure undergoes a pre-displacement of 30 $\mu$m in step-2. **d** The phononic band structure for elastic waves propagating in the $z-$direction is shown for Step-1 ($\alpha$, $\beta$ and $\gamma$ correspond to the structure subjected to a pre-displacement of 0 $\mu$m, 10 $\mu$m and 20 $\mu$m, respectively). **e** The phononic band structure for elastic waves propagating in the $z-$direction is shown for a pre-displacement 30 $\mu$m, i.e., for Step-2. **f** The frequency range of the first band gap is plotted as a function of the pre-displacement.

Herein, based on the principle of local resonance[41], physically concentrated masses are added at the nodes connecting elliptical rings in the $z-$ direction, as shown in Fig. 5**a**. The essential property of the physically concentrated masses is that they change the dynamic mechanical properties of the metamaterial without changing its static mechanical properties. This type of mass can be fabricated with the same raw material as the structure, implying that limited challenges are added to the manufacturing process. If a pre-displacement of 30 $\mu$m is applied in the $z-$direction, the structure deforms from Step-1 (in Fig. 5**b**) to Step-2 (in Fig. 5**c**). At the transition between the steps, the outer surfaces of the curved beams in the $z-$ direction contact with their neighbors as discussed previously.

The phononic band structure for elastic waves propagating along the $z-$ direction is shown in Fig. 5**d**. As apparent in Fig. 5**d**-$\alpha$, the first band gap of the structure appears in the range between 255 kHz and 285 kHz. It does not shift significantly with the pre-displacement within Step-1, as exemplified by panels Fig. 5**d**-$\beta$ and $\gamma$. The first band gap however shifts to the range between 885 kHz and 955 kHz when a pre-displacement of 30 $\mu$m is applied to the structure along the $z-$ direction, i.e. by more than a factor three, as shown in Fig. 5**e**. To prove that the band gap shift from Fig. 5**d** to **e** is introduced by the multi-step behavior of the metamaterial rather than by the pre-stress of each curved beam, the evolution of the phononic band structure under different pre-displacements is compared in Fig. 5**d**. Obviously, within Step-1 the frequency range of the first band gap does not change significantly with the pre-displacement. The observed changes are attributed mainly to the pre-stress of each curved beam. In Step-2, however, the variation of the first band gap is introduced by the contact between curved beams. As a note, it exceeds the mere change of effective velocity at low frequency implied by the static measurement of Young's modulus reported in Fig. 4.

The results demonstrated in this subsection suggest potential applications of the studied metamaterials in dynamics. First, elastic wave dispersion relies on both the added physical concentrated masses and on the mechanical properties of the original structure (the structure studied in the last subsection), implying a high degree of design flexibility. Second, after fabrication variable dispersion properties are obtained only via external compression excitation. This feature decreases the requirements on the operating environment needed to obtain adjustable dispersion behaviors. Finally, during the compression process, the metamaterial does not occupy any additional space thanks to its auxeticity. Hence this type of metamaterial could be used in micro/nanosystems or space-limited devices.

### 4.4 Delocalization of Deformations and Re-usability of the Metamaterial

Structures and materials hardly keep constant mechanical properties and thus remain reusable after undergoing cycles of large deformations. This is usually due to two essential elements, elastoplasticity and the failure mode of the materials. Localized deformations of structures and materials lead to downright failure. Examples are the collapse of lightweight porous structures (or the post-bulking or the instability of their elements), the shear banding in metallic materials, and the propagation of cracks in ceramics. The aforementioned localized deformations limit applications to small strain scenarios. From the mechanical point of view, the occurrence of the initial peak or of the first negative stiffness event in a strain-stress curve implies unstable deformation. Specifically, for periodically porous structures, the localized deformation of the random layer is an indication of a systemic level instability or failure[63].

To obtain reusable 3D mechanical metamaterials, we fabricated the designed metamaterial with thermoplastic urethane (TPU) using the selective laser sintering (SLS) 3D printing technology at the centimeter scale, as shown in Fig. 6**a**. For TPU, Young's modulus is 27 MPa, Poisson's ratio is 0.45, density is 1200 kg/m$^3$, and the elongation of the raw material is 500%. A cycle of five compressive tests with 60% compression strain was employed to evaluate the reusable mechanical response of the metamaterial. After the compressive tests, the loss of the metamaterial is limited, as Fig. 6**b** shows. The responses and deformations are reported in Fig. 6**c**-**h**. To describe the effective properties precisely, the slope of the curves is averaged between $0-40\%$ and $40-60\%$ compression strain to compute the effective properties for each step, as reported in Figs. 6**d** and **f**. Although the curves show slight nonlinearity, the initial peak or the first negative stiffness event is never observed. The effective Poisson's ratio changes from -0.08 to -0.13 between Step-1 and Step-2, whereas Young's modulus concurrently changes from 0.20 MPa to 1.62 MPa.

The metamaterial exhibits stable auxeticity and positive stiffness under large compression deformation, i.e., the corresponding compression strain reaches 60%. These results can be explained based on the delocalization of deformations inside the metamaterial that occurs thanks to its multi-step behavior. Different mechanism-based multi-step behaviors can lead to localized[64] or delocalized[63] response of metamaterials. As a matter of fact, the multi-step behavior presented in this work averts the occurrence of localized deformations of the metamaterial thanks to the self-contact of the outer surfaces of the elliptical rings eliminating instabilities of curved beams, which is a property that matte geometries lack[48]. Significantly, the variations of the effective Poisson's ratio and modulus with TPU show less nonlinearity than their counterparts with the photopolymer of the previous subsection. This highlights the importance of the choice of raw material. Another important point is that the critical strain separating Step-1 and Step-2 depends on the length of the connector between each curved beam in the $z$-direction, i.e., on the parameter $t_c$. If the value of parameter $t_c$ is large enough, the outer surface of the elliptical rings along the $z$-direction will

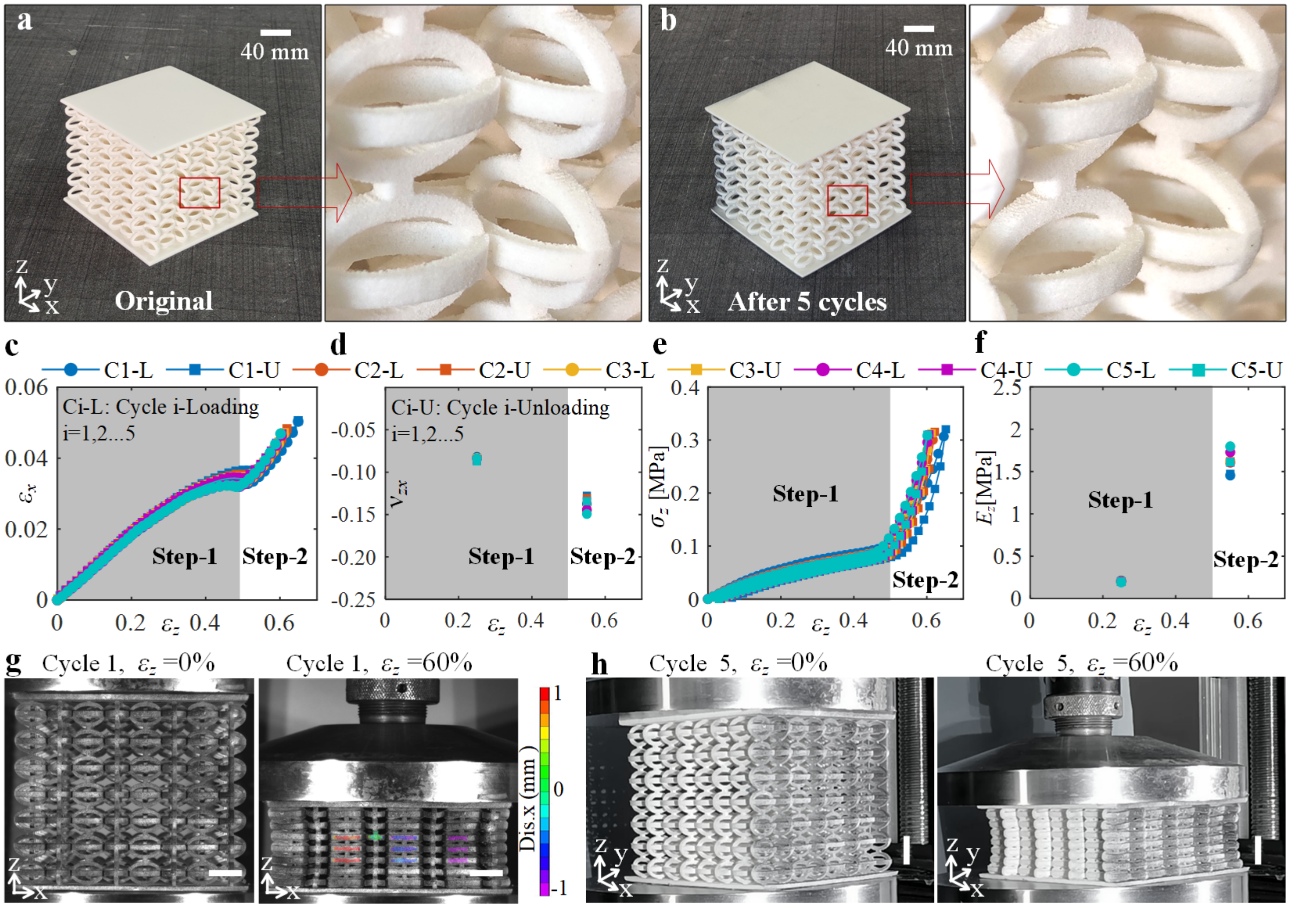

**Figure 6.** Delocalization of deformations and re-usability under large compressive strain. **a** The original metamaterial composed of $4 \times 7$ unit cells was fabricated by TPU. The geometry parameters are set as $a = 9$ mm, $t = 2$ mm, $b = 3$ mm, $t_c = 1$ mm, and $m = n = 1.59$. **b** The metamaterial after five compression tests. **c** Normalized strain $\varepsilon_x$ versus normalized strain $\varepsilon_z$. **d** Effective Poisson's ratio. **e** Normalized stress $\sigma_z$ versus normalized strain $\varepsilon_z$. **f** Effective Young's modulus. C*i*-L(U), *M*=1,2...5, represents the loading (L) or unloading (U) curves of the *i*th cycle. **g-h** Deformation of the metamaterial under different compressive strains and cycles (**g** for the first cycle and **h** for the fifth cycle). The length of the scale bar is 20 mm. The pictures in panel **g** are output from a commercial Digital Image Correlation (DIC) software and the nephogram indicates the displacement along the $x-$direction.

never contact their neighbors during the entire compression process. Under this circumstance, the multi-step behavior will be eliminated. On the contrary, contact can be accelerated by diminishing parameter $t_c$, which means reducing the critical strain between Step-1 and Step-2. Adjustment of this parameter leads to the design flexibility of the multi-step behaviors.

Re-usability of auxetic metamaterials is very important, particularly when they work as functional materials. It here highly relies on the hyperelastic behavior of the raw material TPU. As Figs. 6**c** and **d** show, the auxeticity of the metamaterial remains identical during the 5 cycles. In contrast, Young's modulus in Step-1 of the first cycle is slightly larger than for the subsequent cycles, as shown in Figs. 6**e** and **f**. We think that some initial stress, generated during the fabricating process, is eliminated by the first compression cycle so that the next 4 cycles show a nearly identical effective Young's modulus. The analogous scenario is not observed for auxeticity, since the effective Poisson's ratio of the metamaterial is independent of the properties of the raw material. Figs. 6**g** and **h** demonstrate the deformation of metamaterials from different viewing angles and under a different number of cycles. Fig. 6**g** shows the deformation in the front view during the first cycle while Fig. 6**h** shows the deformation of the side view during the fifth cycle. The nephogram in Fig. 6**g** indicates the displacement along the *x*-direction. The red color in the left region and the purple color in the right region of the sample imply the lateral contraction deformation during compression loading, that is auxeticity of the considered metamaterial. The re-usability of the metamaterial under large compression makes it potentially attractive for applications in some functional fields. For example, the proposed metamaterial can be used many times in engineering fields with time-varying requirements for load-bearing capacity but also lateral and longitudinal space.

## 5 Conclusions

In conclusion, we have introduced a 3D mechanical metamaterial with multi-step mechanical properties under variable applied strain in this paper. The metamaterial has a weaker auxeticity and modulus in Step-1 but stronger counterparts in Step-2. This concept has been demonstrated using a single constituent material structure. Both the instabilities of the elements and the post-buckling of the materials are prevented, which means the whole system remains elastically stable states during the compression process. In addition, the transformation between the two steps solely depends on the applied compressive strain. The multi-step behaviors of the proposed metamaterial could be used to design periodic structures with tunable phononic band gaps. Finally, the contact-based multi-step behavior avoids the occurrence of instabilities in the curved beams during the delocalization deformation of the metamaterial that occurs under large compression strains. Re-usability of the metamaterial is enabled by the hyper-elastic raw material TPU. This study may spur the development of metamaterial with tunable static mechanical properties and multi-functional applications. In the future, the following two aspects may be taken into account when designing metamaterials with tunable mechanical properties. On the one hand, designing metamaterials with identical expected tunable behavior in all three principal directions could address the anisotropy of the current work. On the other hand, constructing metamaterials with special adjustable mechanical properties both under compression and tension mechanical environment is attractive and valuable.

## References

**1.** Frenzel, T., Kadic, M. & Wegener, M. Three-dimensional mechanical metamaterials with a twist. *Science* **358**, 1072–1074 (2017).

**2.** Soukoulis, C. M., Linden, S. & Wegener, M. Negative refractive index at optical wavelengths. *Science* **315**, 47–49 (2007).

**3.** Milton, G. The theory of composites (cambridge monographs on applied and computational mathematics) cambridge university press. *Cambridge, UK* (2002).

**4.** Kadic, M., Milton, G. W., van Hecke, M. & Wegener, M. 3D metamaterials. *Nat. Rev. Phys.* **1**, 198–210 (2019).

**5.** Chen, Y., Abouelatta, M. A., Wang, K., Kadic, M. & Wegener, M. Nonlocal cable-network metamaterials. *Adv. Mater.* 2209988 (2023).

**6.** Craster, R., Guenneau, S., Muamer, K. & Wegener, M. Mechanical metamaterials. *Reports on Prog. physics. Phys. Soc. (Great Britain)* (2023).

**7.** Coulais, C., Sounas, D. & Alu, A. Static non-reciprocity in mechanical metamaterials. *Nature* **542**, 461–464 (2017).

**8.** Coulais, C., Sabbadini, A., Vink, F. & van Hecke, M. Multi-step self-guided pathways for shape-changing metamaterials. *Nature* **561**, 512–515 (2018).

**9.** Grima, J. N. & Evans, K. E. Auxetic behavior from rotating squares. *J. materials science letters* **19**, 1563–1565 (2000).

**10.** Grima, J. N., Jackson, R., Alderson, A. & Evans, K. E. Do zeolites have negative Poisson's ratios? *Adv. Mater.* **12**, 1912–1918 (2000).

**11.** Grima, J. N. *et al.* Tailoring graphene to achieve negative Poisson's ratio properties. *Adv. materials* **27**, 1455–1459 (2015).

**12.** Ghatak, A., Brandenbourger, M., Van Wezel, J. & Coulais, C. Observation of non-Hermitian topology and its bulk–edge correspondence in an active mechanical metamaterial. *Proc. Natl. Acad. Sci.* **117**, 29561–29568 (2020).

**13.** Coulais, C., Teomy, E., De Reus, K., Shokef, Y. & Van Hecke, M. Combinatorial design of textured mechanical metamaterials. *Nature* **535**, 529–532 (2016).

**14.** Qu, J., Gerber, A., Mayer, F., Kadic, M. & Wegener, M. Experiments on metamaterials with negative effective static compressibility. *Phys. Rev. X* **7**, 041060 (2017).

**15.** Zhang, H. *et al.* Creation of acoustic vortex knots. *Nat. communications* **11**, 3956 (2020).

**16.** Chen, Y., Li, X., Hu, G., Haberman, M. R. & Huang, G. An active mechanical Willis meta-layer with asymmetric polarizabilities. *Nat. communications* **11**, 3681 (2020).

**17.** Wang, Z., Zhang, Q., Zhang, K. & Hu, G. Tunable digital metamaterial for broadband vibration isolation at low frequency. *Adv. materials* **28**, 9857–9861 (2016).

**18.** Antonakakis, T., Craster, R. V. & Guenneau, S. Asymptotics for metamaterials and photonic crystals. *Proc. Royal Soc. A: Math. Phys. Eng. Sci.* **469**, 20120533 (2013).

**19.** Guenneau, S. & Craster, R. V. Fundamentals of acoustic metamaterials. *Acoust. Metamaterials: Negat. Refract. Imaging, Lensing Cloaking* 1–42 (2013).

**20.** Wu, Q., Zhang, X., Shivashankar, P., Chen, Y. & Huang, G. Independent flexural wave frequency conversion by a linear active metalayer. *Phys. Rev. Lett.* **128**, 244301 (2022).

**21.** Chen, Y., Li, X., Scheibner, C., Vitelli, V. & Huang, G. Realization of active metamaterials with odd micropolar elasticity. *Nat. communications* **12**, 5935 (2021).

**22.** Chen, X. *et al.* 3D lightweight mechanical metamaterial with nearly isotropic inelastic large deformation response. *J. Mech. Phys. Solids* **169**, 105057 (2022).

**23.** Chen, X. *et al.* Closed tubular mechanical metamaterial as lightweight load-bearing structure and energy absorber. *J. Mech. Phys. Solids* **167**, 104957 (2022).

**24.** Chen, X. *et al.* Optimal isotropic, reusable truss lattice material with near-zero Poisson's ratio. *Extrem. Mech. Lett.* **41**, 101048 (2020).

**25.** Iglesias Martínez, J. A. *et al.* Experimental observation of roton-like dispersion relations in metamaterials. *Sci. advances* **7**, eabm2189 (2021).

**26.** Tan, X. *et al.* A general strategy for performance enhancement of negative stiffness mechanical metamaterials. *Eur. J. Mech.* **96**, 104702 (2022).

**27.** Zhu, S., Wang, B., Chen, L., Tan, X. & Ma, L. Enhance the energy dissipation ability of sleeve-type negative stiffness structures via a phase-difference mechanism. *Int. J. Mech. Sci.* **213**, 106803 (2022).

**28.** Somers, P. *et al.* The physics of 3d printing with light. *Nat. Rev. Phys.* 1–15 (2023).

**29.** Wegener, M. 3D laser micro-and nanoprinting: 10 years of progress. In *Laser 3D Manufacturing X*, PC124120A (SPIE, 2023).

**30.** Porte, X. *et al.* Direct (3+ 1) d laser writing of graded-index optical elements. *Optica* **8**, 1281–1287 (2021).

**31.** Fan, J. *et al.* A review of additive manufacturing of metamaterials and developing trends. *Mater. Today* **50**, 303–328 (2021).

**32.** Liu, S.-F., Hou, Z.-W., Lin, L., Li, Z. & Sun, H.-B. 3D laser nanoprinting of functional materials. *Adv. Funct. Mater.* 2211280 (2023).

**33.** Baigarina, A., Shehab, E. & Ali, M. H. Construction 3D printing: a critical review and future research directions. *Prog. Addit. Manuf.* 1–29 (2023).

**34.** Moughames, J. *et al.* 3d printed multimode-splitters for photonic interconnects. *Opt. Mater. Express* **10**, 2952–2961 (2020).

**35.** Hu, Z. *et al.* Engineering zero modes in transformable mechanical metamaterials. *Nat. Commun.* **14**, 1266 (2023).

**36.** Wang, L. *et al.* Non-reciprocal and non-newtonian mechanical metamaterials. *Nat. communications* **14**, 4778 (2023).

**37.** Tan, X. *et al.* Odd mechanical metamaterials with simultaneously expanding or contracting under both compression and tension. *Thin-Walled Struct.* 112225 (2024).

**38.** Janbaz, S., Narooei, K., Van Manen, T. & Zadpoor, A. Strain rate–dependent mechanical metamaterials. *Sci. advances* **6**, eaba0616 (2020).

**39.** Fang, X. *et al.* Programmable gear-based mechanical metamaterials. *Nat. Mater.* **21**, 869–876 (2022).

**40.** Milton, G. W. & Willis, J. R. On modifications of Newton's second law and linear continuum elastodynamics. *Proc. Royal Soc. A: Math. Phys. Eng. Sci.* **463**, 855–880 (2007).

**41.** Liu, Z. *et al.* Locally resonant sonic materials. *science* **289**, 1734–1736 (2000).

**42.** Münchinger, A., Hsu, L.-Y., Fürniß, F., Blasco, E. & Wegener, M. 3D optomechanical metamaterials. *Mater. Today* **59**, 9–17 (2022).

**43.** Meng, Z., Liu, M., Zhang, Y. & Chen, C. Q. Multi-step deformation mechanical metamaterials. *J. Mech. Phys. Solids* **144**, 104095 (2020).

**44.** Liang, X., Fu, H. & Crosby, A. J. Phase-transforming metamaterial with magnetic interactions. *Proc. Natl. Acad. Sci.* **119**, e2118161119 (2022).

**45.** Ji, Q. *et al.* 4D thermomechanical metamaterials for soft microrobotics. *Commun. Mater.* **2**, 93 (2021).

**46.** Farzaneh, A., Pawar, N., Portela, C. M. & Hopkins, J. B. Sequential metamaterials with alternating Poisson's ratios. *Nat. communications* **13**, 1041 (2022).

**47.** Dudek, K. K. *et al.* Micro-scale mechanical metamaterial with a controllable transition in the Poisson's ratio and band gap formation. *Adv. Mater.* 2210993 (2023).

**48.** Wang, L. *et al.* 3D auxetic metamaterials with elastically-stable continuous phase transition. *Adv. Sci.* 2204721 (2022).

**49.** Bertoldi, K., Reis, P. M., Willshaw, S. & Mullin, T. Negative Poisson's ratio behavior induced by an elastic instability. *Adv. materials* **22**, 361–366 (2010).

**50.** Babaee, S. *et al.* 3D soft metamaterials with negative Poisson's ratio. *Adv. Mater.* **25**, 5044–5049 (2013).

**51.** Tan, X. *et al.* Single-step-lithography micro-stepper based on frictional contact and chiral metamaterial. *Small* **18**, 2202128 (2022).

**52.** Wang, Y., Li, L., Hofmann, D., Andrade, J. E. & Daraio, C. Structured fabrics with tunable mechanical properties. *Nature* **596**, 238–243 (2021).

**53.** Lakes, R. Foam structures with a negative Poisson's ratio. *Science* **235**, 1038–1040 (1987).

**54.** Evans, K. E. & Alderson, A. Auxetic materials: functional materials and structures from lateral thinking! *Adv. materials* **12**, 617–628 (2000).

**55.** Wang, L. *et al.* Directional instability-driven strain-dependent 3D auxetic metamaterials. *Int. J. Mech. Sci.* **199**, 106408 (2021).

**56.** Wang, L. *et al.* Latitude-and-longitude-inspired three-dimensional auxetic metamaterials. *Extrem. Mech. Lett.* **42**, 101142 (2021).

**57.** Yang, H., Wang, B. & Ma, L. Mechanical properties of 3D double-U auxetic structures. *Int. J. Solids Struct.* **180**, 13–29 (2019).

**58.** Gao, Y., Wei, X., Han, X., Zhou, Z. & Xiong, J. Novel 3D auxetic lattice structures developed based on the rotating rigid mechanism. *Int. J. Solids Struct.* **233**, 111232 (2021).

**59.** Setyawan, W. & Curtarolo, S. High-throughput electronic band structure calculations: Challenges and tools. *Comput. materials science* **49**, 299–312 (2010).

**60.** Ma, G. & Sheng, P. Acoustic metamaterials: From local resonances to broad horizons. *Sci. advances* **2**, e1501595 (2016).

**61.** Cummer, S. A., Christensen, J. & Alù, A. Controlling sound with acoustic metamaterials. *Nat. Rev. Mater.* **1**, 1–13 (2016).

**62.** Christensen, J., Kadic, M., Kraft, O. & Wegener, M. Vibrant times for mechanical metamaterials. *Mrs Commun.* **5**, 453–462 (2015).

**63.** Bauer, J., Kraus, J. A., Crook, C., Rimoli, J. J. & Valdevit, L. Tensegrity metamaterials: Toward failure-resistant engineering systems through delocalized deformation. *Adv. Mater.* **33**, 2005647 (2021).

**64.** Shan, S. *et al.* Multistable architected materials for trapping elastic strain energy. *Adv. Mater* **27**, 4296–4301 (2015).

## Acknowledgements

This work was supported by the National Key Research and Development Program of China (grant number 2022YFB3707800), the EIPHI Graduate School of UBFC [grant number ANR-17-EURE-0002], the French Investissements d'Avenir program, in part by the ANR PNanoBot (ANR-21-CE33-0015) and ANR OPTOBOTS project (ANR-21-CE33-0003), the french RENATECH network and its FEMTO-ST technological facility, the National Natural Science Foundation of China [grant number 11972008], and the China Scholarship Council (grant number 202106120088). L. Wang and X. Niu acknowledge the support of the Hong Kong Research Grants Council (HKRGC) General Research Fund (GRF) 11302920. K.K.D. acknowledges the support of the Polish National Science Centre (NCN) in the form of the grant awarded as a part of the SONATA 18 program, project No. 2022/47/D/ST5/00280.

## Author contributions

L.W. conceived the study and carried out the model design, theoretical derivation, experimental testing, and computational analysis, supervised by B.W., V.L., X.N., and M.K., G.U. prepared samples with 3D printing. J.A.I.M. and K.K.D. built the experimental setup and the FEM model, Y.Z. contributed to the theoretical model. All authors worked together to write and revise the manuscript.

## Competing interests

The authors declare no competing interests.